Journal of Theoretical Biology 634 (2026) 112561

Contents lists available at ScienceDirect

Journal of Theoretical Biology

journal homepage: www.elsevier.com/locate/jtbi

Letter to Editor

Cell–cell adhesion cannot sustain extended follower streams in a minimal non-local model of leader–follower migration

Thomas Jun Jewell[1], Samuel W. S. Johnson[1,*], Ruth E. Baker[2], Philip K. Maini[2]

Wolfson Centre for Mathematical Biology, Mathematical Institute, University of Oxford, Oxford, United Kingdom

ARTICLE INFO

Keywords:
Continuum model
Leader–follower migration
Collective cell migration
Cell–cell adhesion
Non-local aggregation

ABSTRACT

Cell–cell adhesion is widely hypothesised to maintain cohesion within the long streams of follower cells that trail leader subpopulations during collective migration, including in neural crest cell migration, angiogenesis, and cancer cell invasion. Mathematically, non-local advection–diffusion equations provide the canonical continuum framework within which to study such adhesive cell–cell interactions. Here, we study a minimal model of leader–follower migration within this framework, in which leaders migrate at constant velocity while followers are attracted to leaders and to one another over a finite spatial interaction range. Numerical simulations reveal that, although the model can maintain small cohorts of travelling follower cells, the size of these cohorts is limited by the adhesive interaction lengthscale and is far below what is needed to reproduce the extended streams observed *in vivo*. Our results highlight a structural limitation of the standard non-local adhesion formulation and thus the need for the development of extended continuum models capable of sustaining long, coherent migratory streams through purely mass-conserving collective cell movement.

1. Introduction

Collective motion is widespread across biology, from flocking birds (Farine, 2022) and schooling fish (Lopez et al., 2012) to the coordinated migration of cells *in vivo* (Rørth, 2009). A recurring feature of such systems is *leader–follower* dynamics, in which a small subset of individuals (leaders) directs the movement of a much larger population (followers). In multicellular systems, leader–follower migration underpins key processes including embryonic development (Scarpa and Mayor, 2016), wound healing (Li et al., 2013), and tumour cell invasion (Friedl et al., 2004). *In vivo*, leader cells migrate in response to external guidance cues such as chemotactic, durotactic, or haptotactic gradients (SenGupta et al., 2021), while follower cells coordinate their motion through interactions with neighbouring cells (Mishra et al., 2019). This leads to the formation of large, connected streams of follower cells trailing leader subpopulations. A canonical example of this phenomenon is chick cranial neural crest cell migration, wherein leader cells respond to gradients in vascular endothelial growth factor and follower cells migrate collectively behind them, with cell–cell adhesion hypothesised to maintain cohesion within streams (McLennan et al., 2012). From a mathematical modelling perspective, such spatially extended streams present a challenge as they persist over distances far greater than the range of direct cell–cell interactions.

Spatially extended migratory fronts arise naturally in mathematical models that include cell proliferation. Classical reaction-diffusion models such as the Fisher-KPP equation produce travelling waves in which cell density behind the advancing front remains high (Murray, 2002; Simpson and McCue, 2024). Similar mechanisms have been proposed in the context of neural crest migration in the gut. For example, continuum partial differential equation models (Simpson et al., 2006, 2007) have predicted that proliferation at the migratory wavefront of neural crest streams drives invasion of the developing gut, a prediction later supported by tissue graft experiments in quail (Simpson et al., 2007). However, in other systems, including the chick cranial neural crest, proliferation is relatively low during the early phases of migration (Ridenour et al., 2014). In such settings, the formation and maintenance of follower streams must be driven by cell–cell interactions that induce movement, rather than by proliferation. Chemotaxis-based continuum models, for example that of Uçar et al. (2025), have been proposed to explain follower migration in such contexts, but typically assume that cells can sense arbitrarily small chemical gradients. Explaining how spatially extended streams emerge without proliferation or long-range

* Corresponding author.
E-mail address: samuel.johnson@maths.ox.ac.uk (S.W.S. Johnson).
[1] These authors contributed equally and share first authorship.
[2] These authors contributed equally and share senior authorship.

https://doi.org/10.1016/j.jtbi.2026.112561
Received 16 April 2026; Received in revised form 10 July 2026; Accepted 27 July 2026
Available online 3 August 2026

gradient sensing, therefore, presents a significant and open modelling challenge.

Cell–cell adhesion is frequently proposed as a mechanism for coordinating follower motion in such systems (McLennan et al., 2012). A canonical and widely used continuum framework for modelling such interactions utilises non-local advection–diffusion equations, also known as non-local aggregation equations, to represent the evolution of interacting cell populations (Armstrong et al., 2006; Carrillo et al., 2019; Painter et al., 2024b). In this framework, the direction of cell migration depends on cell-density gradients sensed over a finite range, reflecting the inherently non-local nature of cell–cell interactions. This formulation captures the fact that cells can attract or respond to neighbouring cells across finite distances through adhesive, chemical, or mechanical cues. Such models have proven remarkably versatile in the study of collective cell behaviours, reproducing a wide repertoire of multicellular patterning (Carrillo et al., 2019; Giunta et al., 2025).

A notable example illustrating the power of this framework is provided by Carrillo et al. (2019), who showed that this class of models can reproduce, both qualitatively and quantitatively, the sorting and mixing of cell subpopulations driven by differential adhesion, as measured experimentally by Katsunuma et al. (2016). More broadly, non-local advection–diffusion models have been applied across developmental and pathological contexts, providing mechanistic explanations for cell aggregation during development (Yu et al., 2026; Jewell et al., 2023; Painter et al., 2015) and forming the basis for representing cell–cell adhesion in a range of processes including cancer invasion (Domschke et al., 2014; Gerisch and Chaplain, 2008; Painter et al., 2010), vasculogenesis (Villa et al., 2022), and skeletal morphogenesis (Glimm et al., 2014). For an extensive review of these models, see Painter et al. (2024b).

Accordingly, the non-local advection–diffusion framework provides a canonical continuum description of cell–cell adhesion and therefore a natural setting in which to study leader–follower migration. However, an unresolved question in this context is whether models based solely on co-attraction and adhesion between proximal cells can sustain streams of follower cells that are both motile and span distances far greater than the typical range of cell–cell interactions. Previous analyses have shown that such models can produce stationary clusters whose extent exceeds the interaction lengthscale of cells (Potts and Painter, 2024; Jewell et al., 2025), or travelling pulses whose size remains limited by that lengthscale (Carrillo et al., 2018; Painter et al., 2024a; Jewell et al., 2025), yet long, cohesive streams of migrating followers have not, to our knowledge, been reported.

To address this question, we study a minimal mathematical model of leader–follower migration formulated within the non-local advection–diffusion framework. Leader cells are prescribed to migrate at a constant velocity in a one-dimensional domain, representing directed motion in response to external cues, while follower cells move according to short-range attractive interactions with both leaders and other followers (Fig. 1).

2. Methods

We study a minimal continuum model of leader–follower migration on a one-dimensional domain of 2000 μm in length. The model comprises two cell populations, leaders and followers, each represented by a continuously varying density along the length of the domain. Leaders and followers each evolve in time according to a system of coupled partial differential equations (PDEs). The leader PDE prescribes movement in the positive x-direction at a fixed speed, v_0, representing migration according to local micro-environmental cues, in processes such as chemotaxis. Conversely, the follower PDE contains terms representing movement according to random diffusive motion, reflecting undirected motility with diffusivity D_f, and short-range, non-local attraction to both leaders and other followers, representing the adhesive and co-attractive interactions commonly cited as key mechanisms for follower cell migration. This effectively extends previous work by Potts (2025), which examined population organisation around a stationary resource, to the case of a moving resource, here represented by the leaders. Follower–follower and follower–leader interactions are parameterised by the non-negative interaction strength coefficients μ_{ff} and μ_{fl}, respectively, and by an interaction lengthscale, ξ, that determines the typical distance over which cells can sense and interact with one another. Here, we take ξ to be the same for follower–follower and follower–leader interactions, as such interactions are often mediated by intrinsic properties of follower cells, such as the length of actin-based protrusions extended at their membrane, or the density of ligand receptors along their membrane. This assumption has also been made in a previous model of non-local leader–follower interactions (Painter et al., 2024a). Follower motion is also subject to a volume-filling constraint, which prevents overcrowding when the combined leader–follower density approaches a constant, κ.

Under these assumptions, the evolution of the leader and follower cell densities, $\rho_l(x,t)$ and $\rho_f(x,t)$, in the domain $x \in [0, L]$ where $L = 2000\,\mu$m, is governed by the PDEs

$$\begin{aligned} \frac{\partial \rho_l}{\partial t} &= -v_0 \frac{\partial \rho_l}{\partial x}, \\ \frac{\partial \rho_f}{\partial t} &= D_f \frac{\partial^2 \rho_f}{\partial x^2} - \frac{\partial}{\partial x}\left(\rho_f (\kappa - \rho_l - \rho_f) \frac{\partial C}{\partial x}\right), \end{aligned} \tag{1}$$

where C is the non-local attraction potential, incorporating follower–follower and leader–follower interactions,

$$C(x,t) = \mu_{ff} \int_0^L K_\xi(x-y)\,\rho_f(y,t)\,\mathrm{d}y + \mu_{fl} \int_0^L K_\xi(x-y)\,\rho_l(y,t)\,\mathrm{d}y. \tag{2}$$

The kernel, $K_\xi(x)$, specifies how the strength of co-attraction or adhesion changes with the distance between cells, and is taken as an even, non-negative Gaussian function:

$$K_\xi(x) = \begin{cases} \alpha(\xi) \exp\left(-\dfrac{x^2}{2\xi^2}\right), & |x| \le 3\xi, \\ 0, & |x| > 3\xi, \end{cases} \tag{3}$$

truncated at 3ξ to ensure compact support while retaining over 99% of the Gaussian mass. The factor $\alpha(\xi)$ ensures that

$$\int_{\mathbb{R}} K_\xi(x)\,\mathrm{d}x = \xi, \tag{4}$$

such that, unlike many continuum representations of non-local adhesion, we do not normalise the kernel $K_\xi(x)$ independently of ξ. Here, the total mass of the kernel scales proportionally with ξ, reflecting the modelling assumption that increasing the interaction range introduces additional interactions rather than diluting the same interactions over a larger distance. Simulations using alternative interaction kernels, including top-hat and Hookean spring-type functions, display qualitatively similar behaviour, suggesting that the results are qualitatively robust to the choice of kernel.

To focus exclusively on the dynamics of cells within the domain, boundary conditions are chosen to prevent any influx of cells at the domain boundaries. The follower diffusion term satisfies homogeneous Neumann (zero-flux) boundary conditions, while the non-local interaction terms are evaluated by extending both leader and follower densities to zero beyond the domain boundaries. The leader population undergoes pure advection to the right, with cells exiting through the right-hand boundary removed and the newly exposed region at the left-hand boundary assigned zero density, corresponding to an absorbing boundary condition. The initial leader and follower profiles are positioned sufficiently far from both boundaries that the peak of the leader pulse never reaches the right-hand boundary during the simulations, ensuring that boundary effects are negligible. Further details of the model and the numerical scheme with which these equations are solved can be found in Appendix A with the corresponding model code available at https://github.com/SWSJChCh/continuumLeaderFollower.

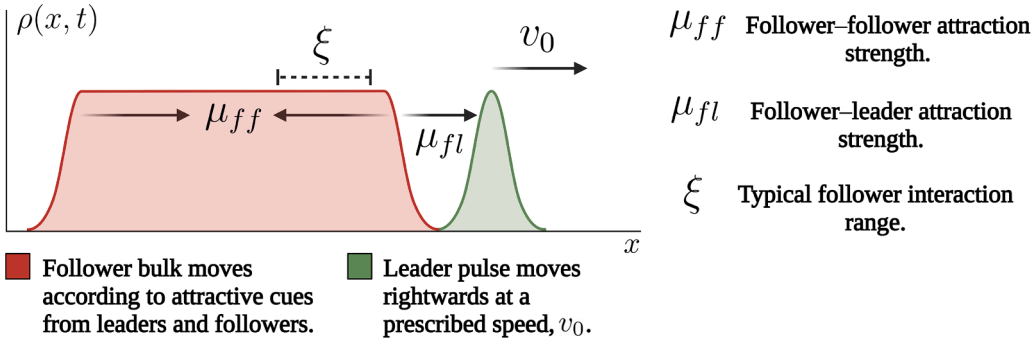

Fig. 1. Mathematical model schematic. The model represents leader and follower populations as continuous densities in a one-dimensional domain. Leader cells migrate in the positive x-direction with a constant speed, v_0, representing migration according to gradients in external cues. Follower cells move according to an integro-partial differential equation, with terms representing diffusion and attractive cues from leader cells and other follower cells. Follower–follower and follower–leader interaction strengths are modulated by the parameters μ_{ff} and μ_{fl}, respectively, while the typical length over which follower–follower and follower–leader interactions occur is represented by the parameter ξ. Created in BioRender by S.W.S. Johnson: https://BioRender.com/dofhwnp.

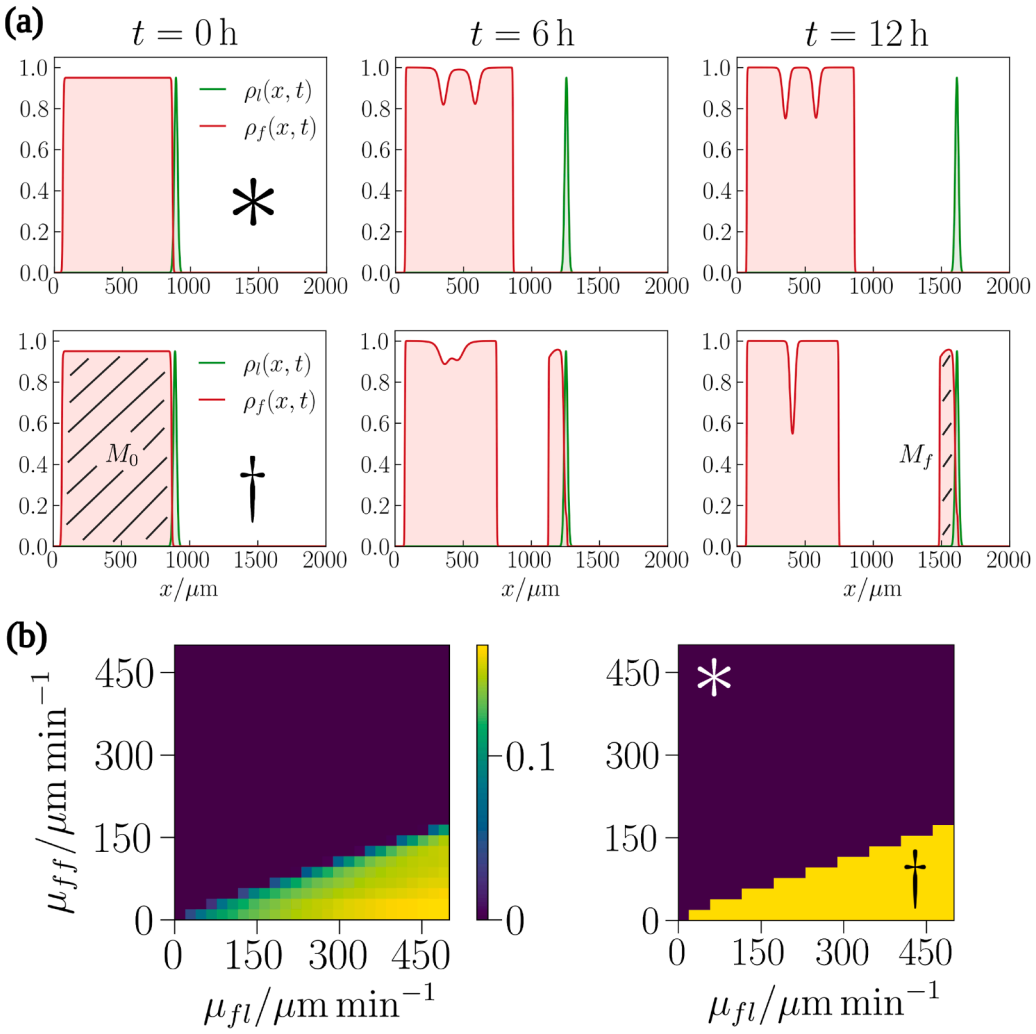

Fig. 2. **(a)** Model simulations for $(\xi, \mu_{ff}, \mu_{fl}) = (50\,\mu\mathrm{m}, 20\,\mu\mathrm{m\,min}^{-1}, 20\,\mu\mathrm{m\,min}^{-1})$ (upper) and $(50\,\mu\mathrm{m}, 20\,\mu\mathrm{m\,min}^{-1}, 200\,\mu\mathrm{m\,min}^{-1})$ (lower), shown at 0 h, 6 h, and 12 h. In the upper panel, follower–follower and leader–follower attraction strengths are equal. Under these conditions, follower cells (red) remain tightly bound, and the attraction exerted by leader cells (green) is insufficient to detach followers from the initial cluster. In the lower panel, follower–leader attraction is increased to ten times the follower–follower attraction. As a result, followers located within the initial interaction range of leaders are rapidly advected towards leaders, while those outside of this range remain in the bulk due to comparatively low follower–follower attraction strength. In the lower panel, M_0 denotes the initial mass of the follower cluster and M_f, the final mass advected with the leaders. **(b)** Heatmaps showing M_f/M_0 for $\xi = 50\,\mu$m across a range of follower–follower and follower–leader interaction strengths. The left heatmap reveals two distinct regimes: (∗) a regime in which follower–follower attraction is sufficiently strong to maintain cluster integrity but followers do not migrate, and (†) a regime in which strong leader–follower attraction advects only those followers within the leaders' initial interaction range. The right heatmap provides a binary classification of these regimes.

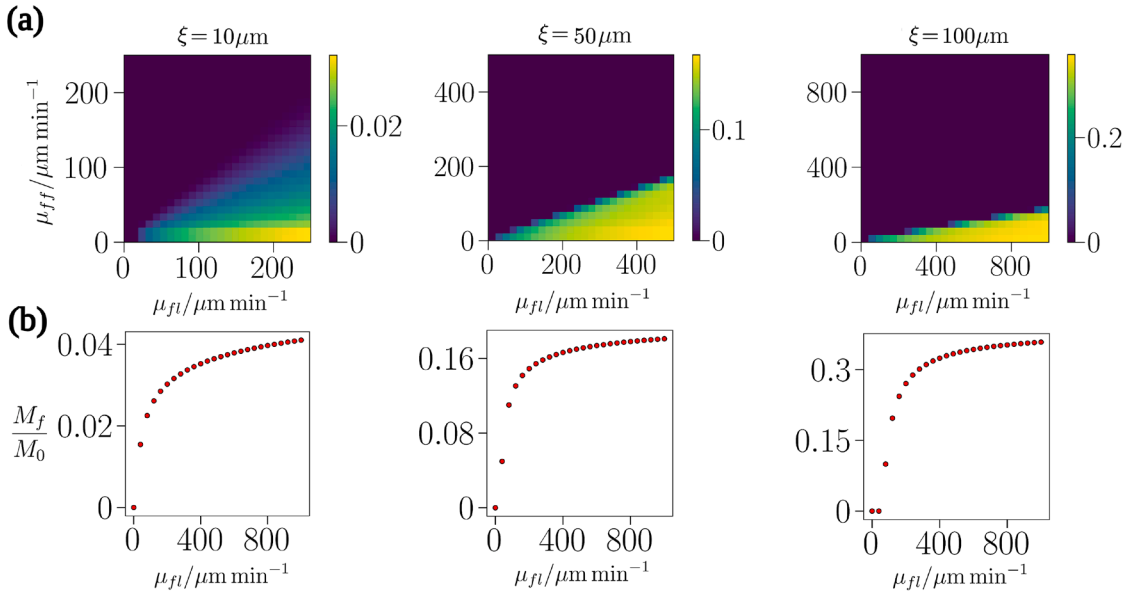

Fig. 3. **(a)** Heatmaps of M_f/M_0 for $\xi = 10\,\mu\text{m}, 50\,\mu\text{m}, 100\,\mu\text{m}$ for a range of interaction strengths. Heatmaps show the existence of two regimes in (μ_{ff}, μ_{fl}) space: a regime in which follower–follower attraction is sufficiently strong to maintain cluster integrity but followers do not migrate, and a regime in which strong leader–follower attraction advects only those followers within the leaders' initial interaction range. **(b)** Line plots of M_f/M_0 as a function of μ_{fl} for fixed $\mu_{ff} = 10\,\mu\text{m min}^{-1}$. Line plots show a gradual plateau in M_f/M_0 as μ_{fl} is increased, indicating a fundamental limit on the degree to which long follower chains may be created.

At the beginning of each simulation, leaders are initialised as a narrow cluster positioned closely ahead of a bulk of follower cells that extends over several hundred micrometres (Fig. 2(a)). Leaders then advance with a constant velocity of $1\,\mu\text{m min}^{-1}$ for a period of 12 h, while followers disperse, interact, and reorganise according to Eq. (1). Parameter values of the model are chosen to represent typical chick cranial neural crest cell dynamics *in vivo* (McLennan et al., 2012). Follower diffusivity is fixed at $D_f = 10\,\mu\text{m}^2\,\text{min}^{-1}$, leader speed at $v_0 = 1\,\mu\text{m min}^{-1}$, and follower interaction lengthscales, ξ, range from approximately one to ten cell lengths ($10\,\mu$m to $100\,\mu$m). Across all simulations, we impose a carrying capacity of $\kappa = 1$, which corresponds to the maximum permitted follower cell density at any point in the domain. This value lies slightly above the maximum initial density of leader and follower cells across the domain, providing a biologically meaningful limit on cell–cell aggregation while permitting aggregates to form. The interaction strengths, μ_{ff} and μ_{fl}, are varied systematically to explore the extent to which follower–follower and follower–leader adhesion and co-attraction facilitate the formation of extended streams of follower cells migrating as a collective behind leader cells.

To quantify the extent to which each parameter set, $(\xi, \mu_{ff}, \mu_{fl})$, facilitates the formation of follower streams, we compare the mass of the main contiguous region of follower density directly behind the leaders after migration ends (M_f) to the initial mass of followers in the domain (M_0) (Fig. 2(a)). This ratio provides a measure of leader–follower migratory efficiency, quantifying the fraction of follower mass that is successfully transported across the tissue segment by leaders. Our analysis compares follower stream sizes across parameter sets and thus investigates whether the model considered here is sufficient to reproduce the long streams of followers observed *in vivo*. Systematic explorations of parameter space have been used to classify pattern-forming behaviour in related non-local advection–diffusion models (Giunta et al., 2025).

3. Results

We systematically explored the parameter space defined by the interaction strengths (μ_{ff}, μ_{fl}) and interaction lengthscale, ξ, quantifying migratory success by the ratio M_f/M_0 of follower mass transported along the domain with leaders relative to the total follower mass. Parameter sweeps were performed over wide ranges of μ_{ff} and μ_{fl} for $\xi = 10, 50, 100\,\mu$m, representing characteristic interaction lengthscales of approximately one, five, and ten cell lengths, respectively (with interactions extending to 3ξ).

For all values of ξ considered, two distinct dynamical regimes consistently emerged (Fig. 3). In the first regime, follower–follower attraction, μ_{ff}, is sufficiently strong that attraction from leader cells is unable to detach follower cells from the initial bulk, and thus, the entire follower mass remains in place. An example simulation in this regime is shown in the upper panels of Fig. 2(a) and corresponds to the region denoted by $*$ in the binary heatmap shown in Fig. 2(b). In the second regime, strong follower–leader attraction, μ_{fl}, enables followers initially positioned within range of the leaders to move towards them. However, because in this regime follower–follower attraction is comparatively weak, these migrating cells are unable to attract additional followers from the rear of the bulk, leaving the majority of the population behind. An example simulation in this regime is shown in the lower panels of Fig. 2(a) and corresponds to the region denoted by † in the binary heatmap shown in Fig. 2(b). Fig. 2(b) shows a heatmap of M_f/M_0 for $\xi = 50\,\mu$m with regions in which M_f/M_0 is close to zero for large values of μ_{ff} relative to μ_{fl}, and is appreciably positive for smaller values of μ_{ff} relative to μ_{fl}, corresponding to the two regimes described above, respectively. Adjacent to this is a binary heatmap clearly indicating the demarcation of these two regimes (with a threshold value of $M_f/M_0 = 10^{-2}$).

As shown in Fig. 3(b), the fraction of transported follower mass increased monotonically with follower–leader attraction strength μ_{fl}. However, for larger values of this parameter, this increase plateaued, indicating a fundamental limit on the proportion of followers that could be transported along the domain with leaders. The precise saturation level depended on the typical follower interaction range, ξ. For $\xi = 10\,\mu$m, only a very small fraction of follower mass, below 0.05, migrated behind the leaders. For $\xi = 50\,\mu$m, the transported fraction did not exceed 0.2. For $\xi = 100\,\mu$m, the transported fraction reached a maximum of approximately 0.35, such that these simulations consistently yielded the largest mass of follower cells transported for a given set of interaction strengths (μ_{ff}, μ_{fl}) (Fig. 3). Thus, for all parameter ranges considered, the majority of followers failed to migrate. Here, we note that if ξ is further increased, it is possible that a larger mass of follower cells could

be transported along the domain. However, such values of ξ would correspond to cell–cell communication over lengths that are far larger than the typical range of short-range communication or adhesion *in vivo*.

These results show that while the model of cell–cell adhesion considered here can generate small cohorts of followers trailing leaders, it cannot sustain extended streams akin to those observed *in vivo* and that follower cell transport is limited by the maximum length over which followers may interact with other cells.

4. Discussion

Our analysis demonstrates that, within the minimal non-local advection–diffusion framework considered here, short-range follower–follower and follower–leader adhesion are not sufficient to sustain spatially extended, motile follower streams. In the model, the extent of the follower population transported with the leaders remains constrained by the interaction lengthscale over which adhesive forces act. Thus, although the system can generate cohesive follower groups, it does not support the formation of long migrating streams under biologically plausible short-range interactions.

Numerical simulations of the coupled one-dimensional non-local PDE system consistently exhibit two distinct dynamical regimes, determined by the relative magnitudes of the attraction strengths, μ_{ff} and μ_{fl}. When follower–follower attraction is sufficiently strong, the follower population remains bound within its initial bulk, and leader attraction is unable to detach and transport it. By contrast, when follower–leader attraction is sufficiently strong, only those followers initially within the interaction range of leaders are advected forwards, while the remaining follower mass is left behind because follower–follower attraction is too weak to propagate motion through the bulk. In both cases, the transported follower mass is restricted by the finite range of the interaction kernel.

Furthermore, our results show that increasing follower–leader attraction does not remove this limitation. Instead, for a fixed interaction lengthscale, ξ, the transported mass increases only up to a plateau, after which stronger attraction to leaders produces no substantial increase in the size of the migrating follower cohort. The saturation level depends on ξ, but for all values considered it remains bounded away from transport of the full follower population. This indicates that the inability to generate extended streams is an intrinsic feature of the canonical short-range non-local adhesion framework. Additionally, prior work has shown that local fourth-order Cahn–Hilliard models represent a short-range limit of the non-local adhesion model considered here (Falcó et al., 2024), suggesting that such models may also have the same limitation.

As our study is based on a numerical exploration of parameter space, we cannot exclude the existence of isolated parameter values for which the two competing effects balance more delicately. However, the absence of any broad parameter regime supporting extended follower transport suggests that such behaviour, if it exists, is not structurally robust within this model class. Thus, the conclusion should be interpreted primarily as a statement about the minimal model mechanism considered here. Within this framework, changing parameter values can alter the amount of follower mass transported, but does not introduce a mechanism for sustained long-range follower recruitment.

The extent to which this limitation applies to other experimental systems will depend on which biological processes dominate follower transport. The parameter values used here are motivated by cranial neural crest cell migration, but related leader–follower phenomena in wound healing, cancer invasion, and other developmental systems may involve additional mechanisms, including proliferation, extracellular matrix remodelling, substrate-mediated mechanical coupling, or long-range signalling. Such processes could alter the resulting dynamics and may allow extended follower populations to be maintained by mechanisms absent from the present minimal model.

This conclusion does not rule out adhesion as a biologically important process in the formation of follower cohorts. Rather, it suggests that an essential feature may be missing from current continuum representations of cell–cell adhesion. Additional mechanisms, such as anisotropic interactions, longer-range signalling, leaders responding to follower behaviour (Bernardi and Painter, 2025), or coupling to external fields or substrates, may also be required to maintain coordinated motion across large follower populations. Our results point to the open challenge of developing continuum models that can produce long, coherent travelling streams through purely mass-conserving, collective cell movement.

CRediT authorship contribution statement

Thomas Jun Jewell: Writing – review & editing, Writing – original draft, Visualization, Methodology, Investigation, Formal analysis, Data curation, Conceptualization; **Samuel W. S. Johnson:** Writing – review & editing, Writing – original draft, Visualization, Methodology, Investigation, Formal analysis, Data curation, Conceptualization; **Ruth E. Baker:** Writing – review & editing, Supervision; **Philip K. Maini:** Writing – review & editing, Supervision.

Declaration of AI-assisted technologies in the writing process

During the preparation of this work, the authors used an OpenAI large language model to assist with grammar, phrasing, proofreading, and code debugging. After using this tool, the authors reviewed and edited the content as needed and take full responsibility for the content of the published article.

Declaration of competing interest

The authors declare that they have no known competing financial interests or personal relationships that could have appeared to influence the work reported in this paper.

Acknowledgements

The authors would like to thank Professor Raluca Eftimie for a valuable discussion leading to the conception of this study. T.J.J. is supported by funding from the Edmund J. Crampin Scholarship at Linacre College, University of Oxford and the Engineering and Physical Sciences Research Council (EPSRC) (grant number EP/W524311/1). R.E.B. is supported by a grant from the Simons Foundation (MP-SIP-00001828). In conducting this work, the authors used the University of Oxford Advanced Research Computing (ARC) facility. For the purpose of open access, the authors have applied a CC BY public copyright licence to any author accepted manuscript arising from this submission.

Appendix A. Model formulation and numerical scheme

A.1. Numerical scheme

We discretise the domain into $N = 10^4$ mesh points, $\{x_i\}_{i=1}^{N}$ with uniform spacing, $h = L/(N-1)$. The system is integrated explicitly in time using a forward Euler scheme. The time step, Δt, is chosen conservatively to satisfy a von Neumann stability constraint

$$\Delta t \leq \frac{h^2}{2D_f}, \tag{A.1}$$

with an additional safety factor, $\theta \in (0,1)$ (here $\theta = 0.05$), to ensure accurate results, giving a final time step of

$$\Delta t = \theta \frac{h^2}{2D_f}. \tag{A.2}$$

In addition to the diffusive restriction, we verify the CFL condition associated with the taxis flux. The relevant discrete advective velocity is the face velocity used in the finite-volume update,

$$u^n_{i+1/2} = P^n_{i+1/2} \frac{C^n_{i+1} - C^n_i}{h}, \qquad P = \kappa - \rho_l - \rho_f. \tag{A.3}$$

Writing $a^+ = \max(a, 0)$ and $a^- = \min(a, 0)$, the corresponding taxis Courant number is

$$\mathrm{CFL}_{\mathrm{taxis}} = \frac{\Delta t}{h} \max_{n,i} \left[\left(u^n_{i+1/2} \right)^+ - \left(u^n_{i-1/2} \right)^- \right]. \tag{A.4}$$

A conservative bound can be obtained directly from the kernel normalisation. Since

$$\int_{\mathbb{R}} K_\xi(x)\,\mathrm{d}x = \xi,$$

the total variation of the truncated Gaussian kernel, including its jumps at $x = \pm 3\xi$, is

$$\mathrm{TV}(K_\xi) = 2\left[\sqrt{2\pi}\,\mathrm{erf}\left(\frac{3}{\sqrt{2}} \right) \right]^{-1} \approx 0.80, \tag{A.5}$$

independently of ξ. Since the weak derivative of K_ξ has zero total mass, its positive and negative variations are each approximately 0.40. Thus, using $0 \le \rho_l, \rho_f \le \kappa$ and $|P| \le \kappa$, we obtain

$$\max_{n,i} \left[\left(u^n_{i+1/2} \right)^+ - \left(u^n_{i-1/2} \right)^- \right] \lesssim 0.80\,\kappa^2 \left(|\mu_{fl}| + |\mu_{ff}| \right). \tag{A.6}$$

For $\mu_{fl}, \mu_{ff} \in [0, 1000]\ \mu\mathrm{m\,min^{-1}}$ and $\kappa = 1$, this gives

$$\max_{n,i} \left[\left(u^n_{i+1/2} \right)^+ - \left(u^n_{i-1/2} \right)^- \right] \lesssim 1.6 \times 10^3\ \mu\mathrm{m\,min^{-1}}. \tag{A.7}$$

With $h \simeq 0.2\ \mu$m and $\Delta t \simeq 10^{-4}$ min, it follows that

$$\mathrm{CFL}_{\mathrm{taxis}} \lesssim 0.80 < 1. \tag{A.8}$$

Meanwhile, the diffusive Courant number is

$$\mathrm{CFL}_{\mathrm{diff}} = \frac{2D_f \Delta t}{h^2} = \theta = 0.05 < 1. \tag{A.9}$$

Thus, the chosen time step lies below both the diffusion and taxis CFL limits. Moreover, because the two terms are advanced together in a single forward-Euler update, their combined sufficient Courant number is

$$\mathrm{CFL}_{\mathrm{diff}} + \mathrm{CFL}_{\mathrm{taxis}} \lesssim 0.05 + 0.80 = 0.85 < 1. \tag{A.10}$$

A.2. Numerical leader update

Leaders are transported at a speed $v_0\ \mu\mathrm{m\,min^{-1}}$ using a discrete shifting algorithm. The displacement increment per time step is

$$\delta s = \frac{v_0 \Delta t}{h}. \tag{A.11}$$

Let S denote the accumulated displacement. At each time step, S is increased by δs, and whenever $\lfloor S \rfloor$ increases by one, the leader density profile, ρ_l, is shifted by one mesh point in the positive x-direction. This formulation avoids the need for interpolation of the leader density at non-grid-aligned locations, and hence ensures exact local mass conservation throughout simulations.

A.3. Numerical follower update

Followers evolve via explicit forward Euler updates of the form

$$\rho_f^{n+1} = \rho_f^n + \Delta t \left(D_f \Delta_h \rho_f^n - \nabla_h \cdot J^n \right), \tag{A.12}$$

where superscripts denote time and Δ_h denotes a second-order finite-difference Laplacian with homogeneous Neumann boundary conditions. The taxis flux is discretised in conservative finite-volume form, with boundary face fluxes set to zero,

$$J^n_{1/2} = J^n_{N+1/2} = 0. \tag{A.13}$$

Together with the homogeneous Neumann discretisation of the diffusive term, this imposes zero total follower flux through $x = 0$ and $x = L$, and hence preserves the integrated follower mass to a high degree of accuracy. Here, the diffusive and taxis components of the follower flux are set to zero separately. This stronger condition is sufficient, but not necessary, for zero total flux and is imposed for numerical simplicity.

A.4. Discretisation of the taxis flux

The divergence of the taxis flux is discretised using a finite-volume formulation. Gradients of the attraction potential, C, are evaluated at cell faces using centred differences,

$$(\partial_x C)_{i+\frac{1}{2}} = \frac{C_{i+1} - C_i}{h}, \tag{A.14}$$

and the corresponding face velocities are defined by

$$u_{i+\frac{1}{2}} = P_{i+\frac{1}{2}} (\partial_x C)_{i+\frac{1}{2}}, \tag{A.15}$$

where i indexes mesh points and $P_{i+\frac{1}{2}}$ is obtained by the arithmetic averaging of P between adjacent mesh points.

The numerical flux through each cell face is computed using an upwind discretisation,

$$J_{i+\frac{1}{2}} = \begin{cases} \rho_{f,i} u_{i+\frac{1}{2}}, & u_{i+\frac{1}{2}} \ge 0, \\ \rho_{f,i+1} u_{i+\frac{1}{2}}, & u_{i+\frac{1}{2}} < 0. \end{cases} \tag{A.16}$$

The discrete divergence of the flux is then given by

$$(\nabla_h \cdot J)_i = \frac{J_{i+\frac{1}{2}} - J_{i-\frac{1}{2}}}{h}. \tag{A.17}$$

A.5. Non-local convolution

Given a kernel, K_ξ, and a discrete density, Z, the convolution is given by

$$(K_\xi * Z)(x_i) \;\approx\; h \sum_j K_\xi(x_i - x_j) Z(x_j), \tag{A.18}$$

and is computed using a fast Fourier convolution with zero padding beyond the domain boundaries.

A.6. Follower cell diffusion constant

In simulations, we choose a moderate diffusion constant of $D_f = 10\ \mu\mathrm{m^2\,min^{-1}}$ for follower cells. For one hour of migration, this results in a characteristic diffusive lengthscale of

$$\ell(60\,\mathrm{min}) = \sqrt{2\mathrm{D}_f \mathrm{t}} = \sqrt{2 \times 10\,\mu\mathrm{m^2 min^{-1}} \times 60\,\mathrm{min}} = \sqrt{1200}\,\mu\mathrm{m} \approx 35\,\mu\mathrm{m}. \tag{A.19}$$

Thus, with this choice of D_f, the expected spread of a cell over one hour is approximately 3.5 cell lengths ($\sim 35\ \mu$m), though this diffusion is largely attenuated by the follower–follower attraction that is also present in the model.

A.7. Initial conditions

The initial condition consists of a follower bulk trailing a leader pulse

$$\rho_f(x, 0) = \frac{f_0}{2} \left(\tanh \frac{x - x_a^f}{\delta} - \tanh \frac{x - x_b^f}{\delta} \right), \tag{A.20}$$

$$\rho_l(x, 0) = l_0 \exp\left(-\frac{(x - x_0)^2}{2\sigma^2} \right), \tag{A.21}$$

with $0 < x_a^f < x_b^f < x_0 < L$, where $f_0 = l_0 \le \kappa$. In simulations we take $[x_a^f, x_b^f] = [65\ \mu\mathrm{m}, 870\ \mu\mathrm{m}]$, $x_0 = 895\ \mu$m, $\delta = 5\ \mu$m, $\sigma = 12\ \mu$m, and $f_0 = l_0 = 0.95$, yielding a narrow leader peak located just ahead of an extended follower train (Fig. 2(a)).

Although in this work we have considered fixed values of f_0 and l_0, we have verified that our conclusions are robust to variations in both of these parameters. In particular, reducing l_0 is, to a good approximation, equivalent to reducing the effective follower–leader adhesion strength, μ_{fl}, since the leader contribution to the non-local adhesion term is proportional to the leader density, as seen in Eq. (2). Although this equivalence is not exact because of the volume-filling term in Eq. (1), the

correction is small owing to the limited spatial overlap between the two populations. Reducing f_0 likewise has little effect on the long-term dynamics, as follower–follower adhesion rapidly drives aggregation until the local follower density approaches the carrying capacity. Consequently, the qualitative behaviour and principal conclusions of the study are insensitive to the specific initial conditions chosen.

References

Armstrong, N.J., Painter, K.J., Sherratt, J.A., 2006. A continuum approach to modelling cell–cell adhesion. J. Theor. Biol. 243 (1), 98–113.

Bernardi, S., Painter, K.J., 2025. The impact of different degrees of leadership on collective navigation in follower-leader systems. Bull. Math. Biol. 87 (5), 64.

Carrillo, J.A., Huang, Y., Schmidtchen, M., 2018. Zoology of a nonlocal cross-diffusion model for two species. SIAM J. Appl. Math. 78 (2), 1078–1104.

Carrillo, J.A., Murakawa, H., Sato, M., Togashi, H., Trush, O., 2019. A population dynamics model of cell-cell adhesion incorporating population pressure and density saturation. J. Theor. Biol. 474, 14–24.

Domschke, P., Trucu, D., Gerisch, A., Chaplain, M. A.J., 2014. Mathematical modelling of cancer invasion: implications of cell adhesion variability for tumour infiltrative growth patterns. J. Theor. Biol. 361, 41–60.

Falcó, C., Baker, R.E., Carrillo, J.A., 2024. A local continuum model of cell-cell adhesion. SIAM J. Appl. Math. 84 (3), S17–S42. https://doi.org/10.1137/22M1506079

Farine, D.R., 2022. Collective action in birds. Curr. Biol. 32 (20), R1140–R1144.

Friedl, P., Hegerfeldt, Y., Tusch, M., 2004. Collective cell migration in morphogenesis and cancer. Int. J. Dev. Biol. 48 (5-6), 441–449.

Gerisch, A., Chaplain, M. A.J., 2008. Mathematical modelling of cancer cell invasion of tissue: local and non-local models and the effect of adhesion. J. Theor. Biol. 250 (4), 684–704.

Giunta, V., Hillen, T., Lewis, M.A., Potts, J.R., 2025. A phylogeny of biological patterns formed by nonlocal advection. arXiv preprint arXiv:2506.00489.

Glimm, T., Bhat, R., Newman, S.A., 2014. Modeling the morphodynamic galectin patterning network of the developing avian limb skeleton. J. Theor. Biol. 346, 86–108.

Jewell, T.J., Krause, A.L., Maini, P.K., Gaffney, E.A., 2023. Patterning of nonlocal transport models in biology: the impact of spatial dimension. Math. Biosci. 366, 109093.

Jewell, T.J., Krause, A.L., Maini, P.K., Gaffney, E.A., 2025. Chase-and-run and chirality in nonlocal models of pattern formation. Bull. Math. Biol. 87 (11), 160.

Katsunuma, S., Honda, H., Shinoda, T., Ishimoto, Y., Miyata, T., Kiyonari, H., Abe, T., Nibu, K.-i., Takai, Y., Togashi, H., 2016. Synergistic action of nectins and cadherins generates the mosaic cellular pattern of the olfactory epithelium. J. Cell Biol. 212 (5), 561–575.

Li, L., He, Y., Zhao, M., Jiang, J., 2013. Collective cell migration: implications for wound healing and cancer invasion. Burns Trauma 1 (1), 21–26.

Lopez, U., Gautrais, J., Couzin, I.D., Theraulaz, G., 2012. From behavioural analyses to models of collective motion in fish schools. Interface Focus 2 (6), 693–707.

McLennan, R., Dyson, L., Prather, K.W., Morrison, J.A., Baker, R.E., Maini, P.K., Kulesa, P.M., 2012. Multiscale mechanisms of cell migration during development: theory and experiment. Development 139 (16), 2935–2944.

Mishra, A.K., Campanale, J.P., Mondo, J.A., Montell, D.J., 2019. Cell interactions in collective cell migration. Development 146 (23), dev172056.

Murray, J.D., 2002. Biological waves: single species models. In: Mathematical Biology. Springer, pp. 437–483.

Painter, K.J., Armstrong, N.J., Sherratt, J.A., 2010. The impact of adhesion on cellular invasion processes in cancer and development. J. Theor. Biol. 264 (3), 1057–1067.

Painter, K.J., Bloomfield, J.M., Sherratt, J.A., Gerisch, A., 2015. A nonlocal model for contact attraction and repulsion in heterogeneous cell populations. Bull. Math. Biol. 77 (6), 1132–1165.

Painter, K.J., Giunta, V., Potts, J.R., Bernardi, S., 2024a. Variations in non-local interaction range lead to emergent chase-and-run in heterogeneous populations. J. R. Soc. Interface 21 (219), 20240409.

Painter, K.J., Hillen, T., Potts, J.R., 2024b. Biological modeling with nonlocal advection–diffusion equations. Math. Models Methods Appl. Sci. 34 (1), 57–107.

Potts, J.R., 2025. Aggregation–diffusion in heterogeneous environments. J. Math. Biol. 90 (6), 59.

Potts, J.R., Painter, K.J., 2024. Distinguishing between long-transient and asymptotic states in a biological aggregation model. Bull. Math. Biol. 86 (3), 28.

Ridenour, D.A., McLennan, R., Teddy, J.M., Semerad, C.L., Haug, J.S., Kulesa, P.M., 2014. The neural crest cell cycle is related to phases of migration in the head. Development 141 (5), 1095–1103.

Rørth, P., 2009. Collective cell migration. Annu. Rev. Cell Dev. Biol. 25, 407–429.

Scarpa, E., Mayor, R., 2016. Collective cell migration in development. J. Cell Biol. 212 (2), 143–155.

SenGupta, S., Parent, C.A., Bear, J.E., 2021. The principles of directed cell migration. Nat. Rev. Mol. Cell Biol. 22 (8), 529–547.

Simpson, M.J., Landman, K.A., Hughes, B.D., Newgreen, D.F., 2006. Looking inside an invasion wave of cells using continuum models: proliferation is the key. J. Theor. Biol. 243 (3), 343–360.

Simpson, M.J., McCue, S.W., 2024. Fisher–KPP-type models of biological invasion: open source computational tools, key concepts and analysis. Proc. R. Soc. A Math. Phys. Eng. Sci. 480 (2294), 20240186.

Simpson, M.J., Zhang, D.C., Mariani, M., Landman, K.A., Newgreen, D.F., 2007. Cell proliferation drives neural crest cell invasion of the intestine. Dev. Biol. 302 (2), 553–568.

Uçar, M.C., Alsberga, Z., Alanko, J., Sixt, M., Hannezo, E., 2025. Self-generated chemotaxis of mixed cell populations. Proc. Natl. Acad. Sci. 122 (34), e2504064122.

Villa, C., Gerisch, A., Chaplain, M. A.J., 2022. A novel nonlocal partial differential equation model of endothelial progenitor cell cluster formation during the early stages of vasculogenesis. J. Theor. Biol. 534, 110963. https://doi.org/10.1016/j.jtbi.2021.110963

Yu, C., Mederacke, M., Vetter, R., Iber, D., 2026. Directed cell migration is a versatile mechanism for rapid developmental pattern formation. Newton 100557. https://doi.org/10.1016/j.newton.2026.100557